nature chemical engineering

Supplementary information

https://doi.org/10.1038/s44286-024-00110-9

End-of-life tire decontamination from 6PPD and upcycling

In the format provided by the authors and unedited

Crumb rubber particle size distributions were determined using dynamic light scattering (Fig. S1). The larger particles, typically used for recreational fields, were about twice the diameter of the smaller particles. The particle size distributions are normally distributed.

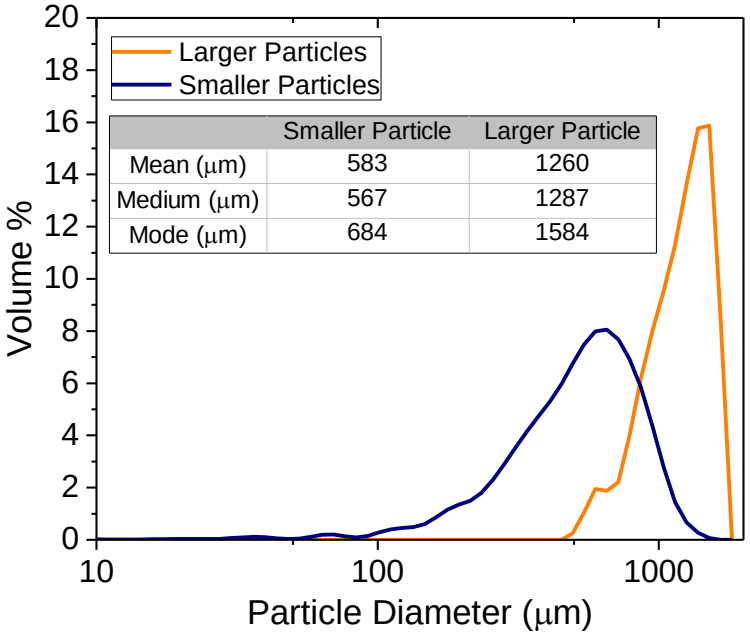

Fig. S1 Particle size distributions of crumb rubber obtained via dynamic light scattering.

The microwave susceptor properties of the 0.6 mm (smaller) and 1.3 mm (larger) particles show a significantly measurable difference between the two (Fig. S2). The microwave properties of this material are due to the carbon black present. When the carbon black powder from the pyrolysis of either particle is analyzed, the dielectric constant and loss factor increase dramatically to 24 and 13, respectively. These values are consistent with what is reported in the literature[16].

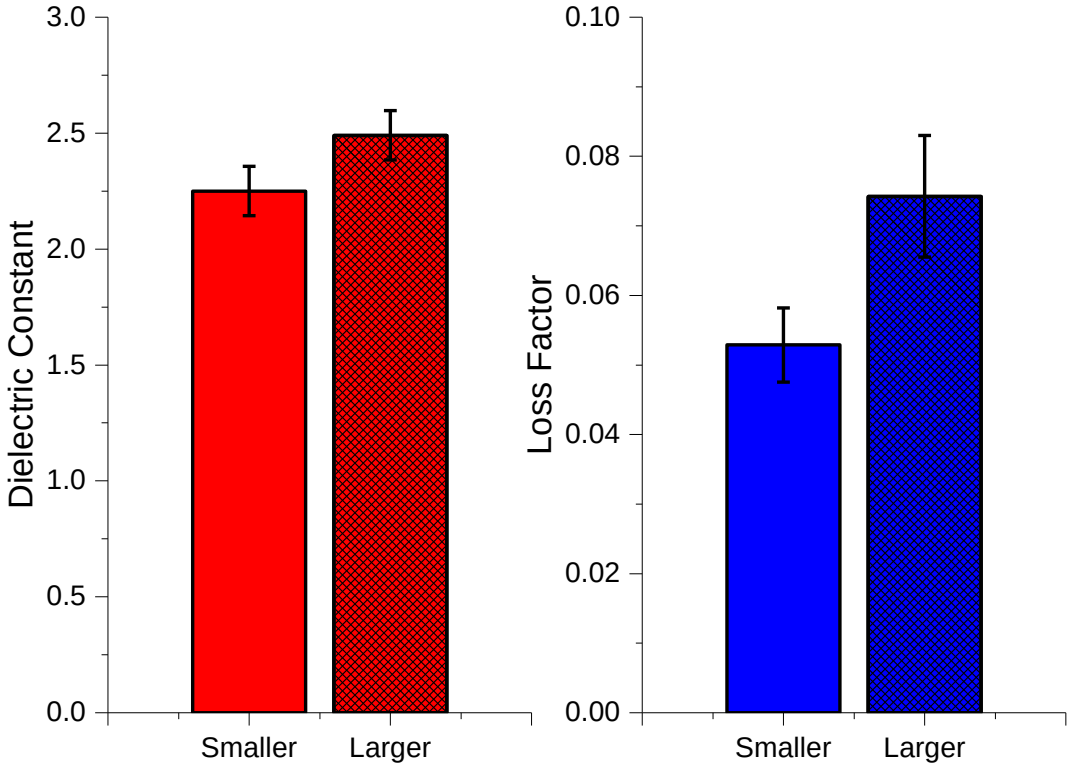

Fig. S2 Dielectric constant and loss factor of the two different crumb rubber particle sizes. Error bars represent the standard error obtained from duplicate runs.

The TGA profiles of the two crumb rubber particle sizes and the smaller, extracted particles are shown in Fig. S3. In Fig. S3A, the combustion of the larger particle has a very different curve shape to the smaller particle. This contrast may be due to heat transfer limitations, which can cause a delay in the combustion of these particles. Some mass left after the combustion can be attributed to ZnO particles, Si-based fillers, and other additives. The TGA curve under an inert N_2 atmosphere is shown in Fig. S3B. The profiles follow similar trends, although the end weight % for each is different. The weight % remaining is higher than in Fig. S3A because the carbon black remains intact. Interestingly, the curves plateau around 475 °C, suggesting this is the temperature required for complete pyrolysis.

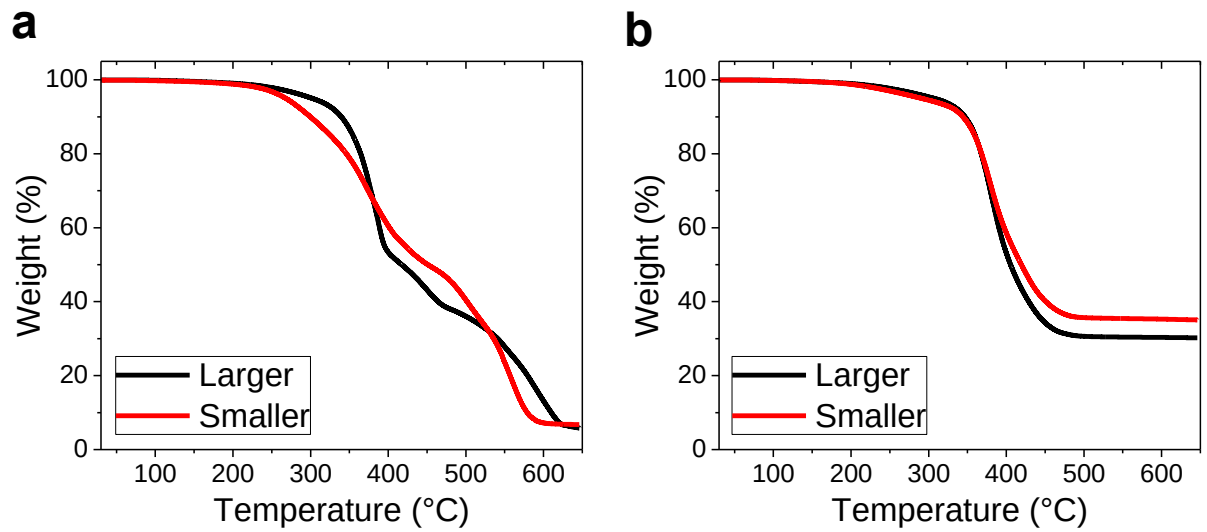

Fig. S3 TGA profile of crumb rubber particles under 20 mL/min (a) air and (b) nitrogen.

The normalized power consumptions from other MW pyrolysis experiments taken in the literature[17–19] are shown in Fig. S4. The values were taken by multiplying the forward power by the reaction time and dividing by the mass of the crumb rubber used. Our work has reduced power consumption relative to the literature studies.

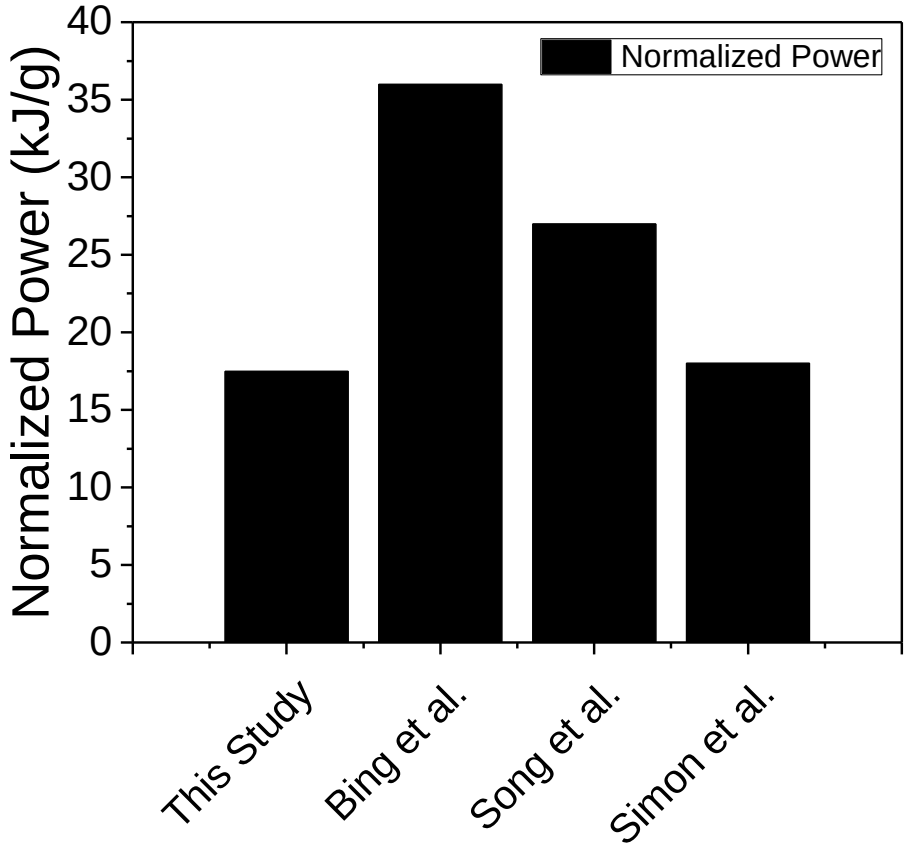

Fig. S4 Normalized power consumption for microwave-assisted pyrolysis of crumb rubber compared to other studies.

Full SEM images of the crumb rubber particles under MW radiation at various times can be found in Fig. S5.

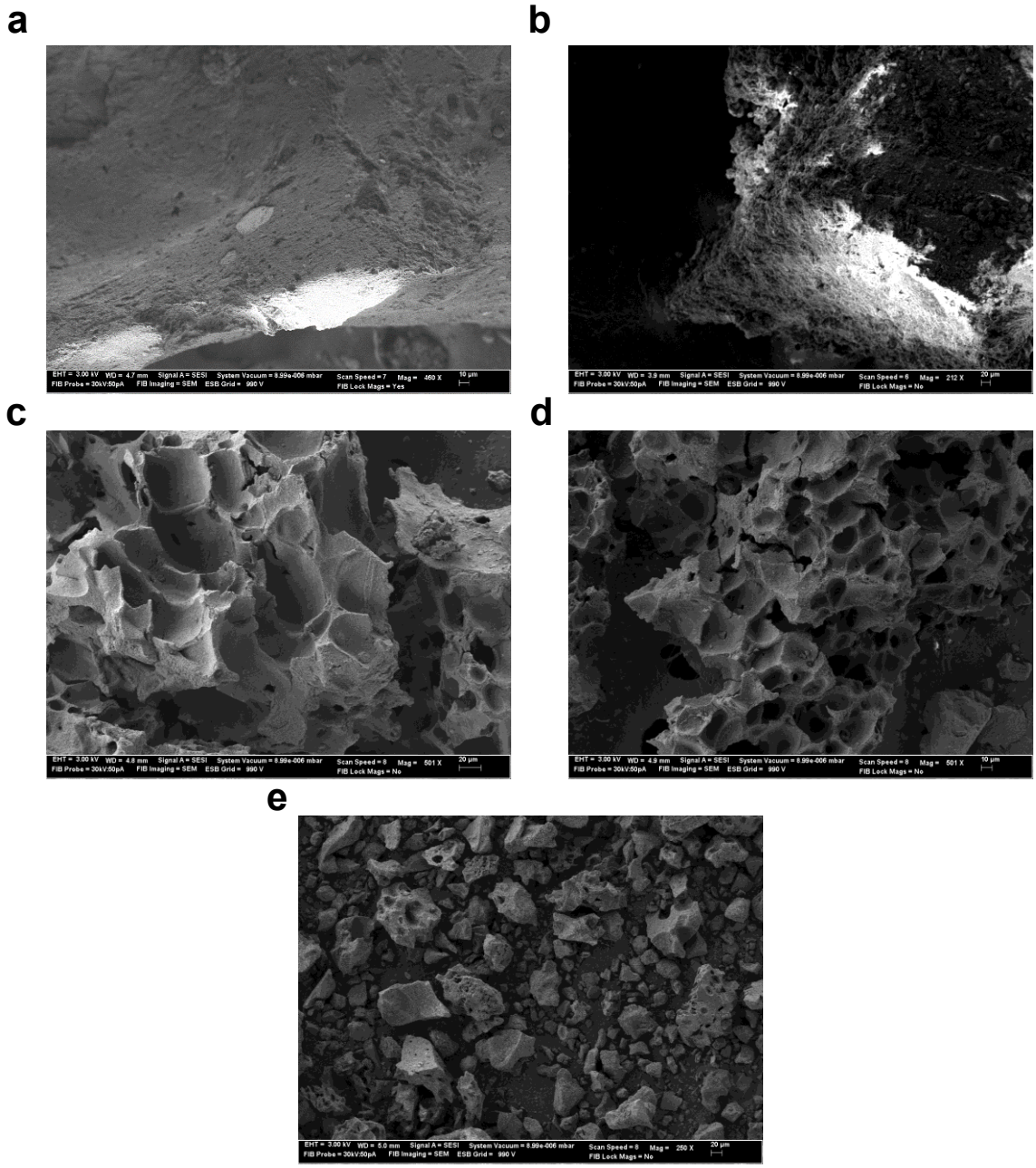

Fig. S5 Full SEM images with magnification details from Figure 1c of main text. Exposure to microwave radiation: a) 0 min b) 1 min c) 2 min d) 3 min e) 10 min.

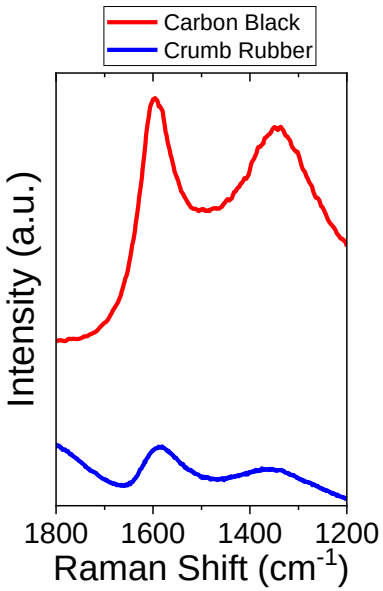

Fig. S6 Raman spectra of carbon black powders obtained from pyrolysis of as received and solvent extracted crumb rubber. The Raman spectra of as received crumb rubber is shown for comparison.

The fresh crumb rubber and the residual carbon black, derived from various sections of the MW-pyrolysis reactor, were characterized using Raman spectroscopy (Fig. S6). All samples exhibited a distinctive G band, indicative of graphitic carbon, and a D-band associated with defected carbon. The ID/IG ratios, as presented in Table S1 consistently indicated that regardless of whether the extraction occurred before or during pyrolysis, the samples closely resembled the fresh crumb rubber, with ID/IG ratios falling within the range of 0.8 - 0.9.

Table S1 ID/IG band ratio from Raman Spectra in **Error! Reference source not found.**.

Sample	ID/IG Ratio
Carbon black	0.84
Crumb Rubber	0.80

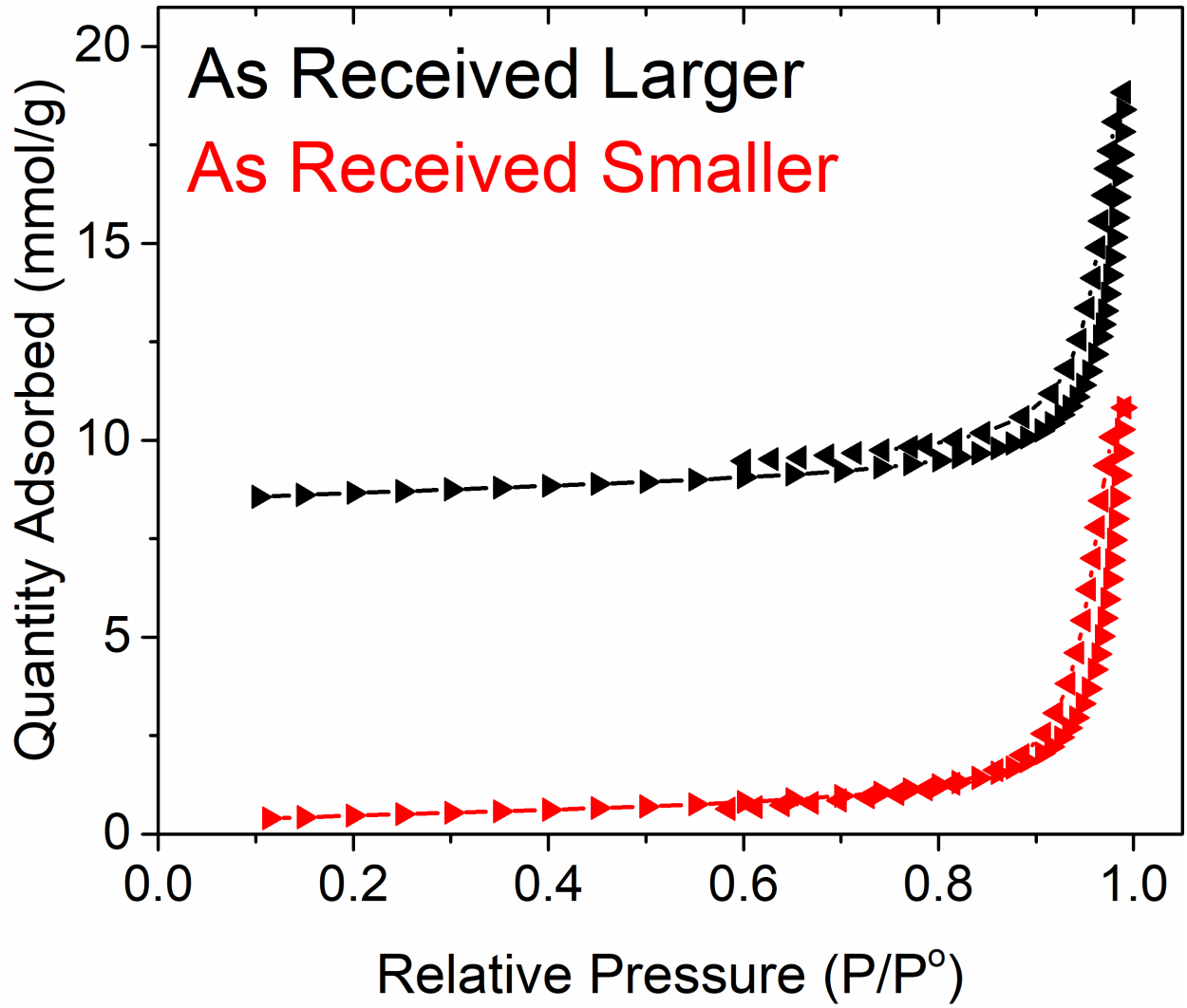

Fig. S7 N_2 Physisorption isotherms of carbon black powders following full pyrolysis. All isotherms have been shifted upward in the y direction for clarity.

The mass % of certain metals present in the starting crumb rubber and carbon black obtained from pyrolysis are shown in Table S2. The contribution of carbon and oxygen cannot be measured via the XRF and is assumed to be equal for these samples. The Zn comes from ZnO, and S is due to the crosslinking present in the rubber phase. Generally, the relative amount of these elements stays the same for each of the samples. The significant amount of sulfur remaining in the solid confirms that most of the aromatic species formed do not contain any sulfur heteroatoms.

Table S2 Mass % of different atoms on the surface of carbon blacks obtained from pyrolysis of as received crumb rubber and the starting crumb rubber itself.

Atom	Starting Crumb Rubber	Carbon Black
Sulfur	19	24
Zinc	56	50
Iron	8	5
Silicon	8	12

The SEM image and EDS mapping of carbon black obtained from the pyrolysis of solvent-extracted crumb rubber particles is shown in Fig. S8. The atoms are evenly dispersed on the carbon black surface. Zinc tends to have a more clustered atom distribution, most likely due to localized ZnO crystals spread on the surface of the carbon black material.

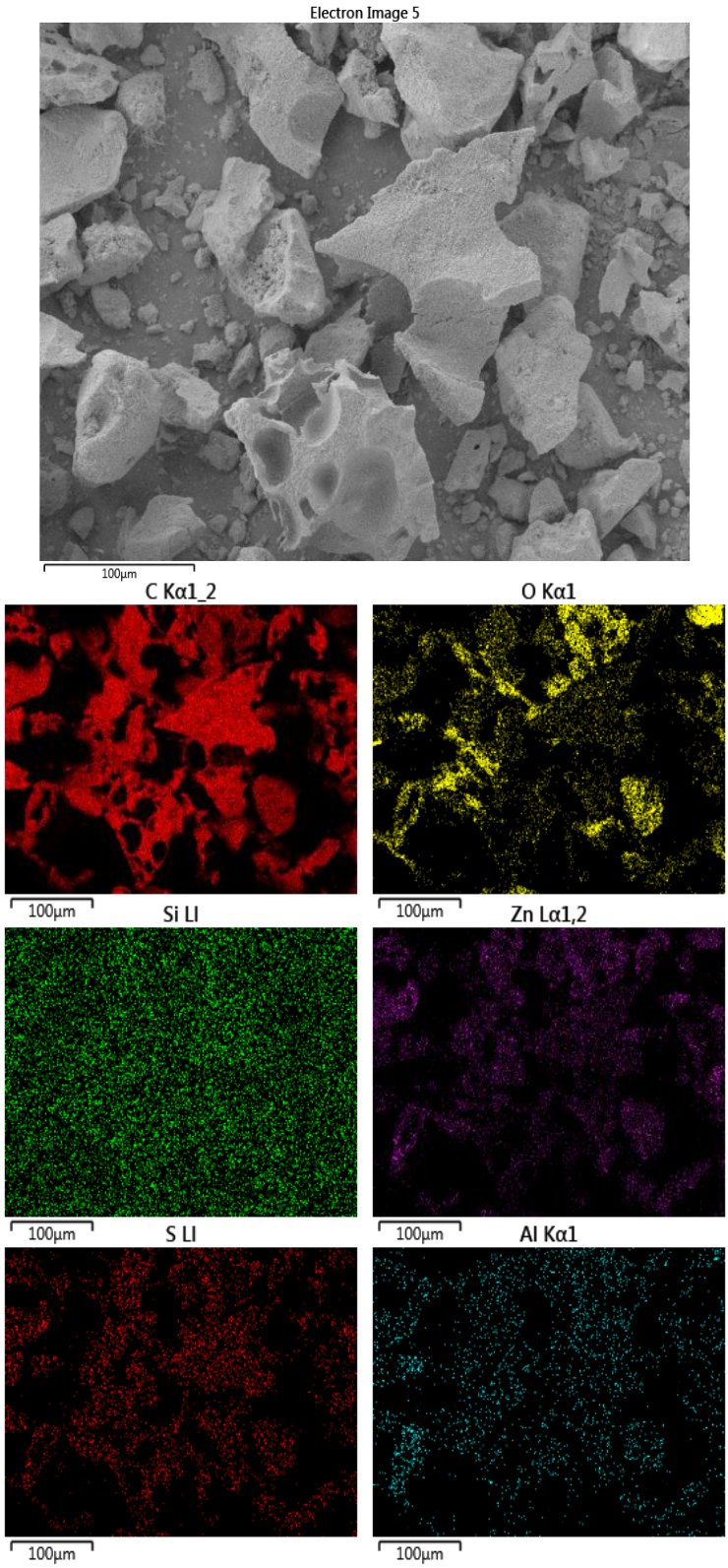

Fig. S8 SEM and EDS mapping of carbon black obtained from fully pyrolyzed crumb rubber.

TGA-MS was performed on the carbon black obtained from pyrolysis (Fig. S9). The figure below demonstrates little organic contamination, as evidenced by the virtual absence of any mass change under nitrogen. When combusted, the carbon black loses >85% of its mass, primarily carbon, as evidenced by the derivative curve following the same pattern as the CO_2 signal.

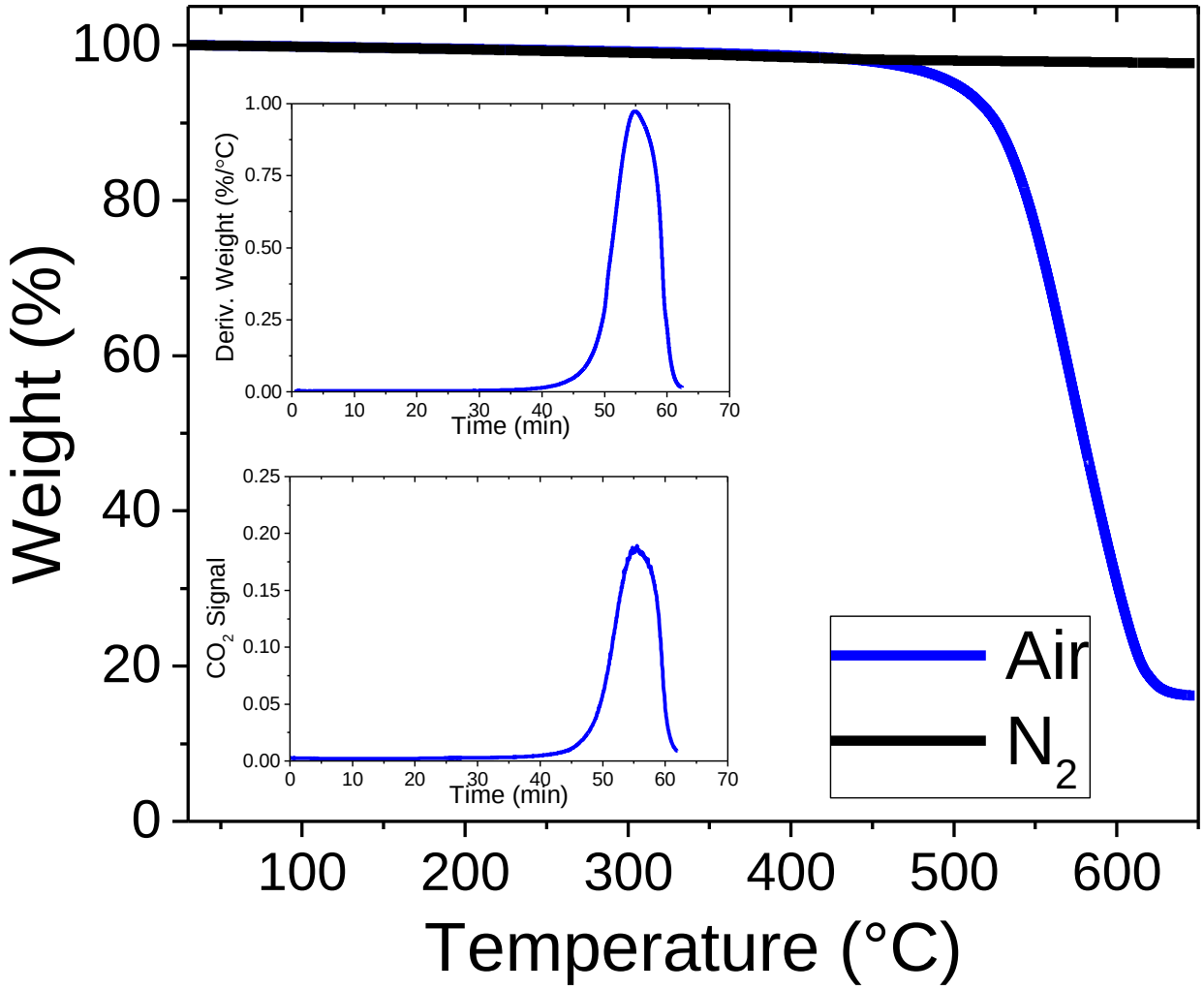

Fig. S9 TGA profile of carbon black obtained from pyrolysis under air and nitrogen. The insets depict the derivative curve and CO2 signal for the air profile.

The GCMS trace from pyrolysis oil obtained via microwave-assisted pyrolysis of as-received shown in Fig. S10 with the peak corresponding to 6PPD labeled. The mass fragmentation pattern from this peak is shown in Fig. S10B with a direct comparison to a reference mass fragmentation pattern.

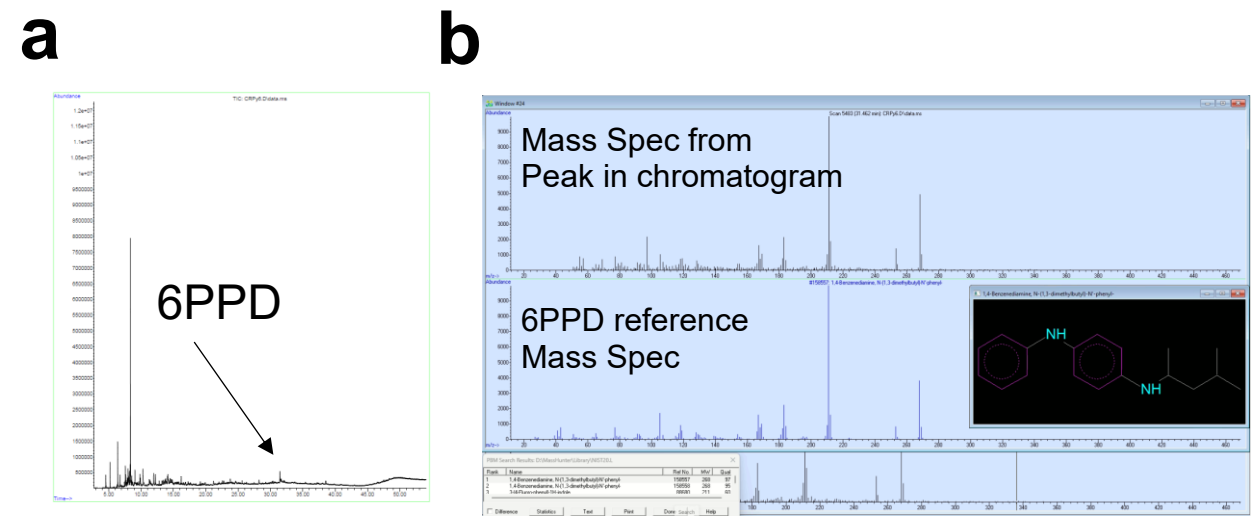

Fig. S10 Chromatogram of pyrolysis oil from pyrolysis of as received crumb rubber (a). The peak indicating the presence of 6PPD in the pyrolysis oil is labeled. The mass spectrum corresponding to the peak labeled in (a) is shown in (b).

The TGA curve of 6PPD is shown in Fig. S11 and shows the degradation of 6PPD does not begin to occur in nitrogen until approximately 200 °C with a maximum degradation at 300 °C.

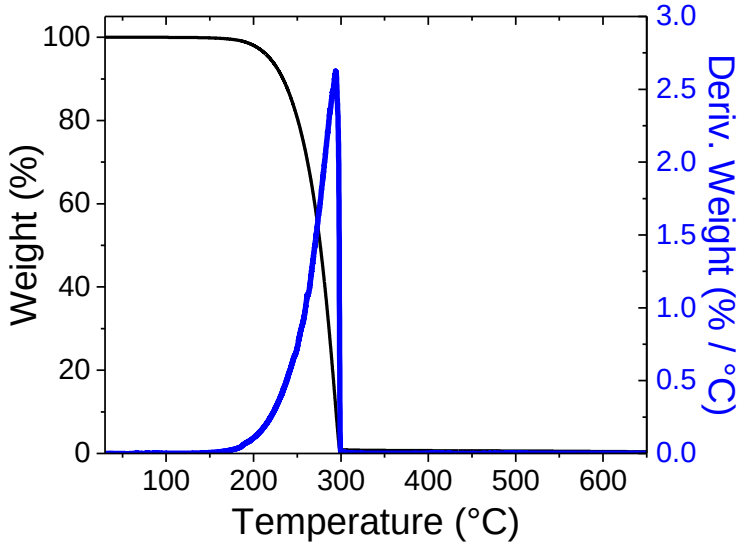

Fig. S11 TGA curve of 6PPD under 20 mL/min of N_2 flow.

The zoomed-in GC trace from Fig. S10B is shown in Fig. S12 with labeled products. D-limonene is the most prominent peak, as it has the highest yield in the oil product (Fig. 1E). The heavier, fused aromatic compounds appear at longer retention times. The corresponding mass fragmentation patterns from peaks in the chromatogram were used to identify products.

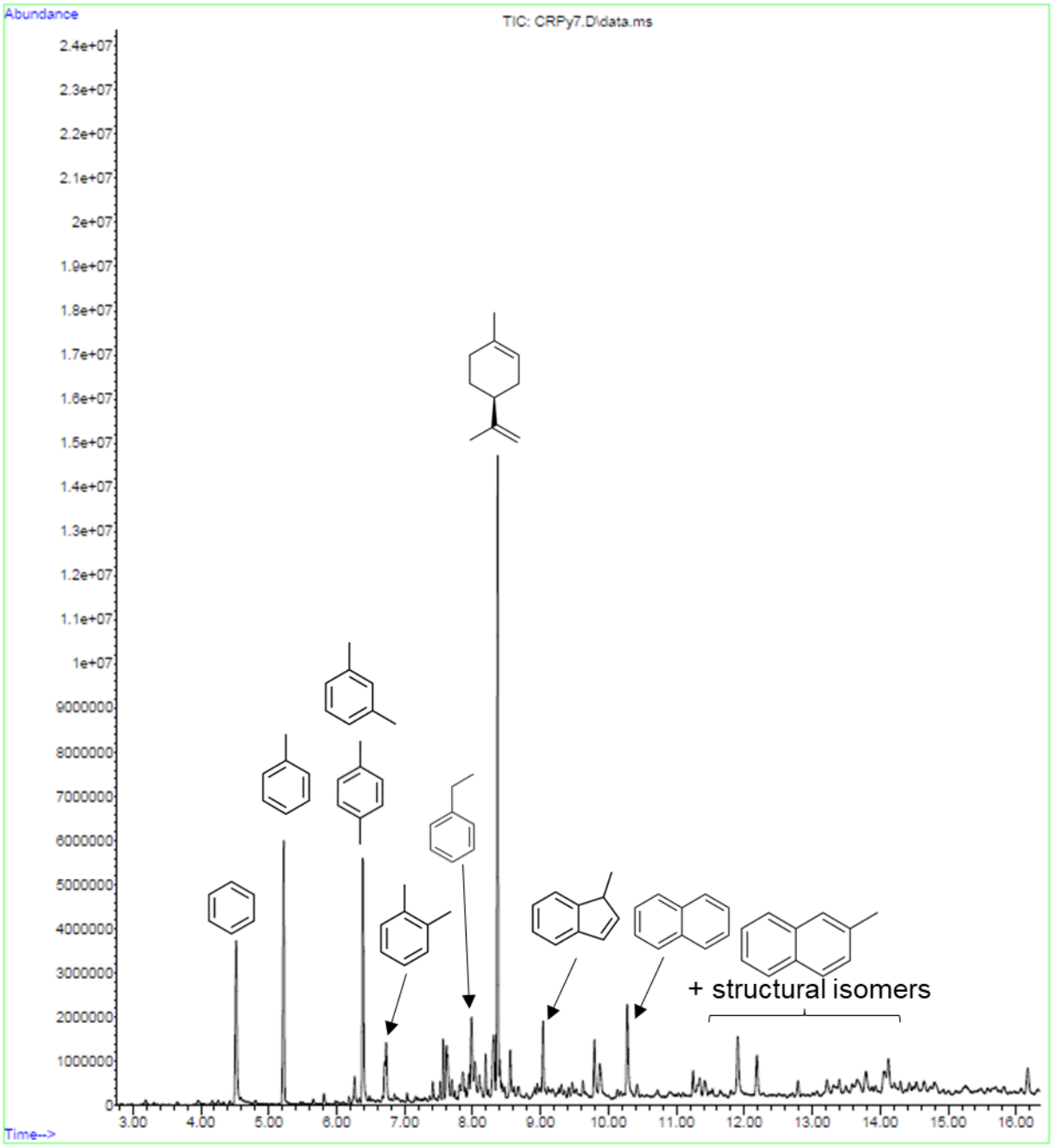

Fig. S12 Gas chromatogram of pyrolysis oil products identified via mass spectrometry.

A first-order rate model was derived using the initial conditions obtained experimentally to fit the initial concentration (Fig. 2B). The model was then fit by minimizing the sum of the square residuals to find the rate constant and maximum concentration (C_S).

$$\frac{dC_t}{dt} = k(C_s - C_t)$$

$$\int_{C_0}^{C_t} \frac{dC_t}{(C_s - C_t)} = \int_0^t k dt$$

$$C_t = C_s(1 - e^{-kt}) + C_0 e^{-kt}$$

Here, C_t is the concentration of 6PPD at time t, k is the first-order rate constant, and C_0 is the initial concentration. Values for k in Fig. 2B are 0.066, 0.031, and 0.028 min^{-1} for cycles 1-3 respectively.

Products detected via GCMS from crumb rubber extraction using ethanol under batch microwave heating are shown in Fig. S13. Several unidentifiable peaks (via MS libraries) suggest proprietary additives from tire manufacturers are present in the crumb rubber.

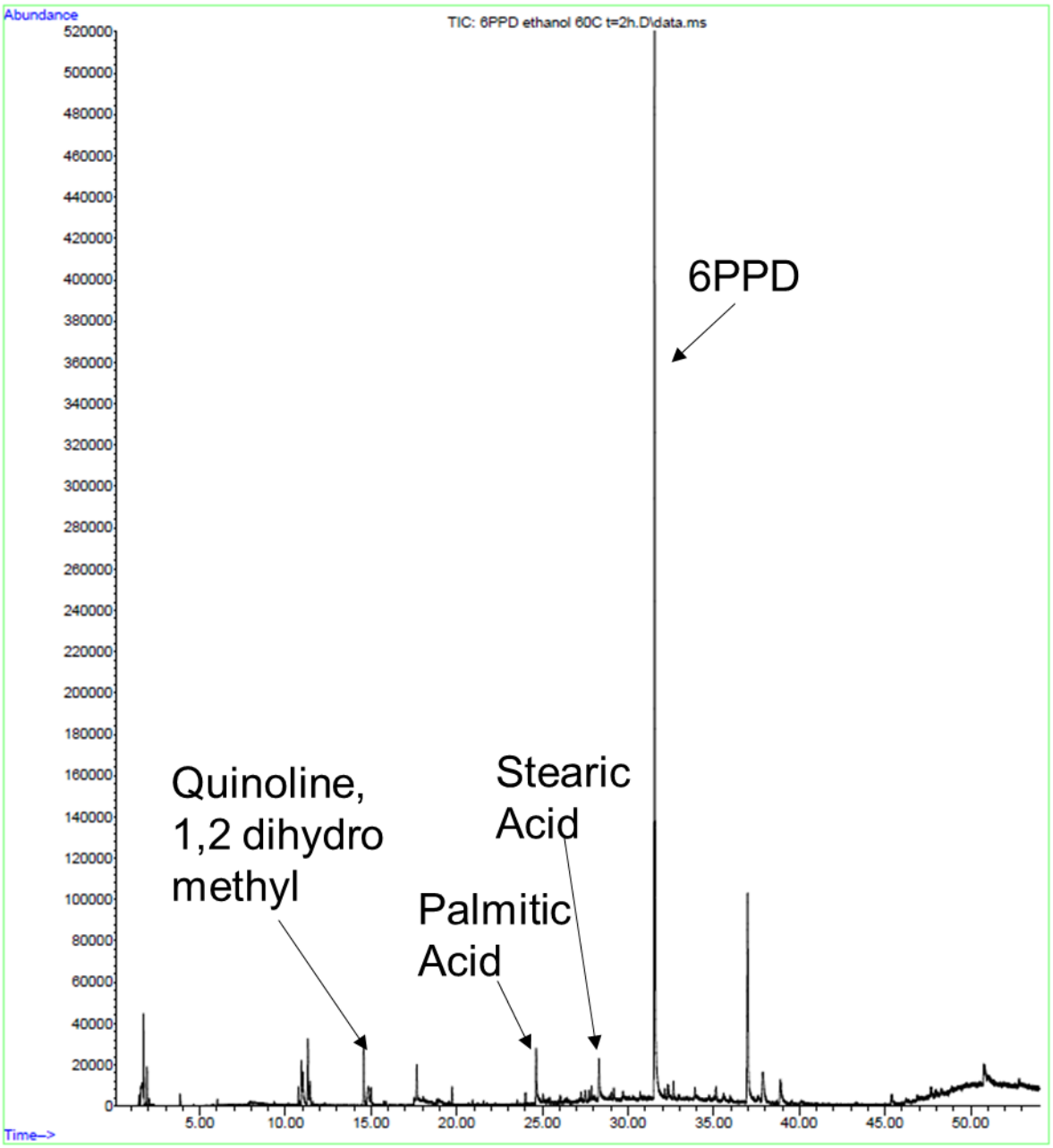

Fig. S13 GCMS results of extract from ethanol batch extraction.

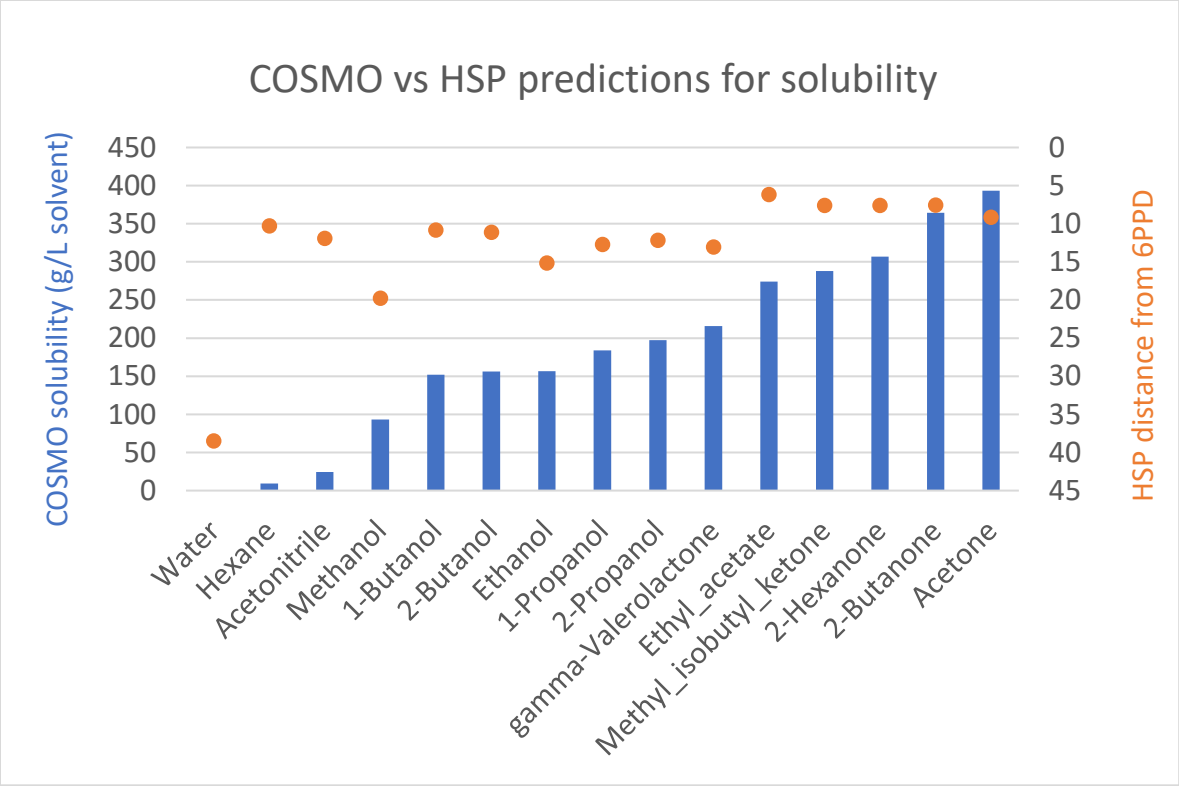

Fig. S14 Comparison of COMSO Solubility and HSP Distances from 6PPD for the various solvents tested.

Table S3. COSMO solubility of 6PPD in tested solvents and HSP distances of 6PPD from each solvent. HSP values for 6PPD are dD = 18.8, dP = 4.1, and dH = 6.3.

Solvent	COSMO Solubility (g/L)	dD	dP	dH	HSP Distance
Water	0.000	15.5	16	42.3	38.5
Hexane	9.4	14.9	0	0	10.8
Acetonitrile	24.5	15.3	18	6.1	15.6
Methanol	93.1	14.7	12.3	22.3	19.8
1-Butanol	152.2	16	5.7	15.8	11.1
2-Butanol	156.3	15.8	5.7	14.5	10.3
Ethanol	156.4	15.8	8.8	19.4	15.2
1-Propanol	183.8	16	6.8	17.4	12.7
2-Propanol	197.4	15.8	6.1	16.4	11.9
Ethyl_acetate	274.1	15.8	5.3	7.2	6.2
Methyl_isobutyl_ketone	288.1	15.3	6.1	4.1	7.6
2-Hexanone	306.7	15.3	6.1	4.1	7.6
2-Butanone	364.6	16	9	5.1	7.5
Acetone	393.5	15.5	10.4	7	9.2

The final temperatures taken at 20 min of applied power for both conventional and applied heating are shown in Fig. S15. Two important things stand out: the first is that MW heating achieves a higher final

temperature than conventional heating, and the trends for each profile are different. While the final temperature using conventional heating follows a linear trend with increasing power, the MW power has an exponential pattern with power vs. final temperature. This aligns with the pyrolysis upshot behavior, where the temperature rapidly increases at a certain power level. The exponential trend also indicates that MW pyrolysis can result in faster temperature climbs.

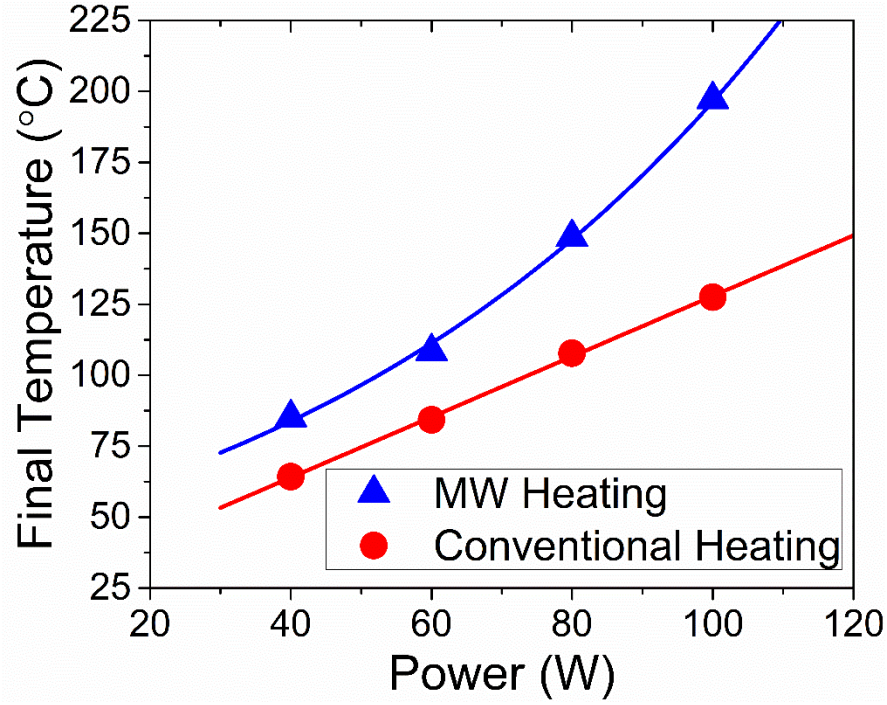

Fig. S15 Comparing MW and conventional heating. Final Temperature under MW and conventional heating as a function of input power supplied and absorbed.

Table S4 displays the atomic weights of the as-received crumb rubber and post-extraction. There is a clear increase in the amount of carbon, hydrogen, and sulfur present in the sample post-extraction. The relative amount of nitrogen has decreased post-extraction suggesting N-containing additives, notably 6PPD, are removed from the sample due to extraction. Residual nitrogen can be due to the carbon support itself as has been seen elsewhere[7].

Table S4 Weight % of C, H, N and S atoms in the starting crumb rubber and solvent extracted crumb rubber from Fig 2Ei.

Atom	C %	H %	N %	S %
As Received	78 ± 1	3.1 ± 0.5	0.40 ± 0.01	1.87 ± 0.07
Extracted	80.3 ± 0.6	5.8 ± 0.2	0.36 ± 0.01	2.35 ± 0.07

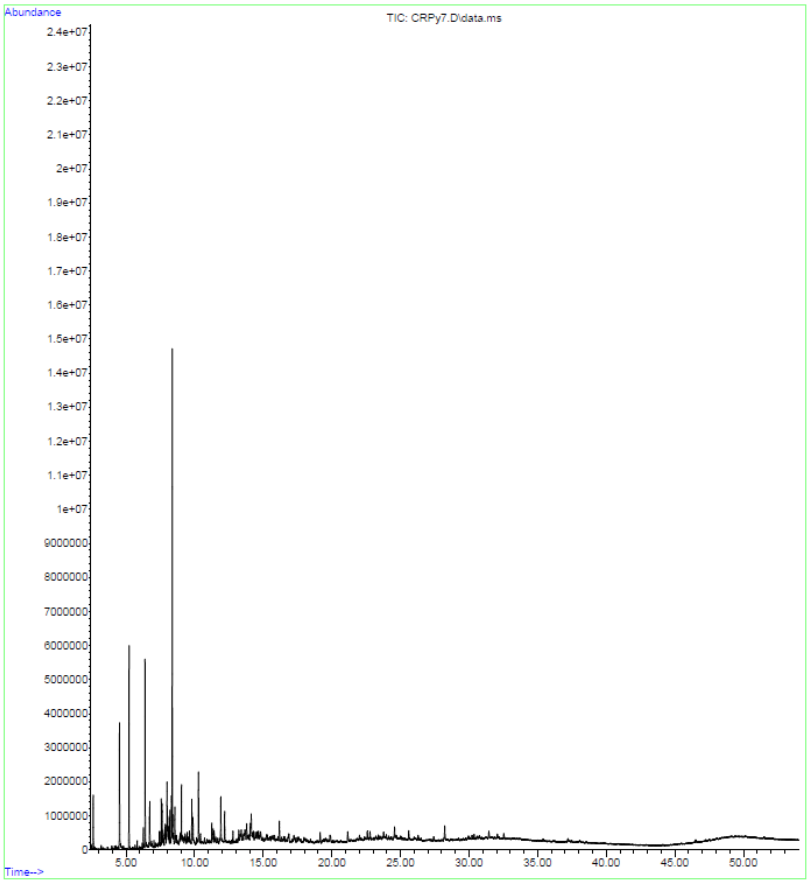

Fig. S16 GC trace from pyrolysis oil product indicating no 6PPD is present at the 31 min retention as appeared in Fig. S10

The lattice spacing of the Pd atoms is shown in Fig. S17. The spacing between the Pd atoms is consistent with the spacing of the inter-planes of the 111 facet of fcc Pd[8].

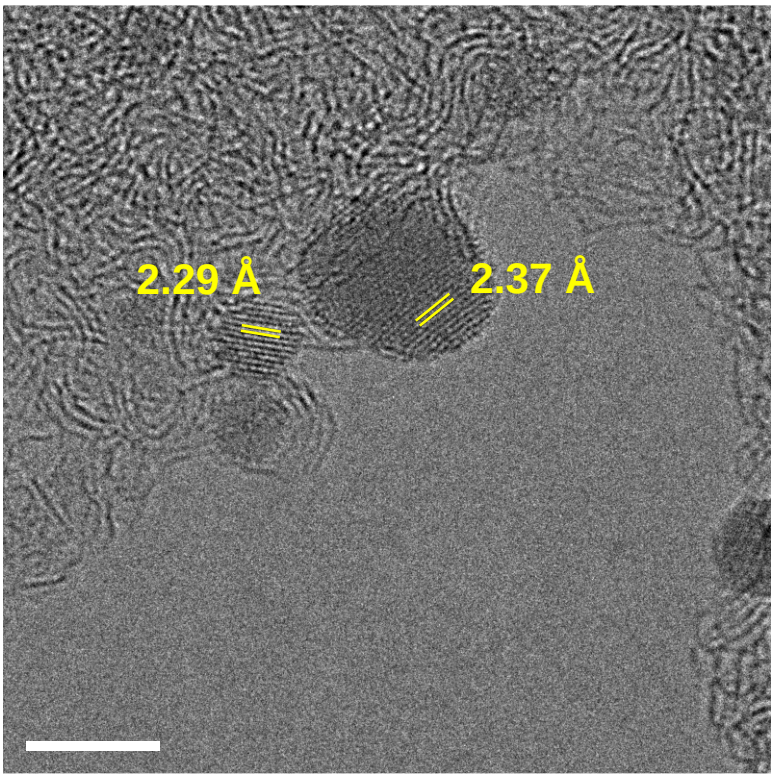

Fig. S17 TEM image of 5 wt% Pd/C catalyst with lattice spacing of Pd atoms marked. The scalebar is 5 nm.

Fig. S18 shows the XPS of the fresh and spent Pd/C catalysts. The XPS in the C1s region indicates the carbon support of the fresh Pd/C (Fig. S18A) is mostly composed of sp^2 and sp^3 carbons (C1 and C2, respectively)[9,10]. The broad tail of the C1s band extends to 294 eV, demonstrating there is also a complex mixture of oxygenated carbon species present[11,12], and corroborated by the O1s region (Fig. S18C) showing high concentrations of quinones (O1), ketones (O2), and keto-enol (O3) functionalities[11,12]. XPS of the Pd3d region (Fig. S18E) reveals 92% of the Pd is present as metallic Pd with minor quantities of oxidized PdO and PdO_2[13–15]. Significant alterations are observed to the C1s, O1s, and Pd3d regions upon reaction. The C1s band (Fig. S18B) of the spent Pd/C catalyst is still primarily composed of sp^2 and sp^3 carbons, but the +0.5 eV shift to higher binding energies suggests a partial reduction of the carbon support with higher sp^3 contributions and corroborated by the decrease in π-π^* satellites (C8) at $\geq$290 eV[9,10]. Furthermore, the concentration of individual oxygenated species also fluctuates, and this redistribution is mirrored in the O1s region with higher concentrations of carbonyl and keto-enol groups while the presence of quinones is suppressed (Fig. S18D). Surprisingly, a +0.7 eV shift in the Pd $3d_{5/2}$ peak position was observed for the spent catalyst (Fig. S18F), with deconvolution revealing a 75% loss in metallic Pd to oxidized species with $Pd^{\delta+}$ accounting for 65%.

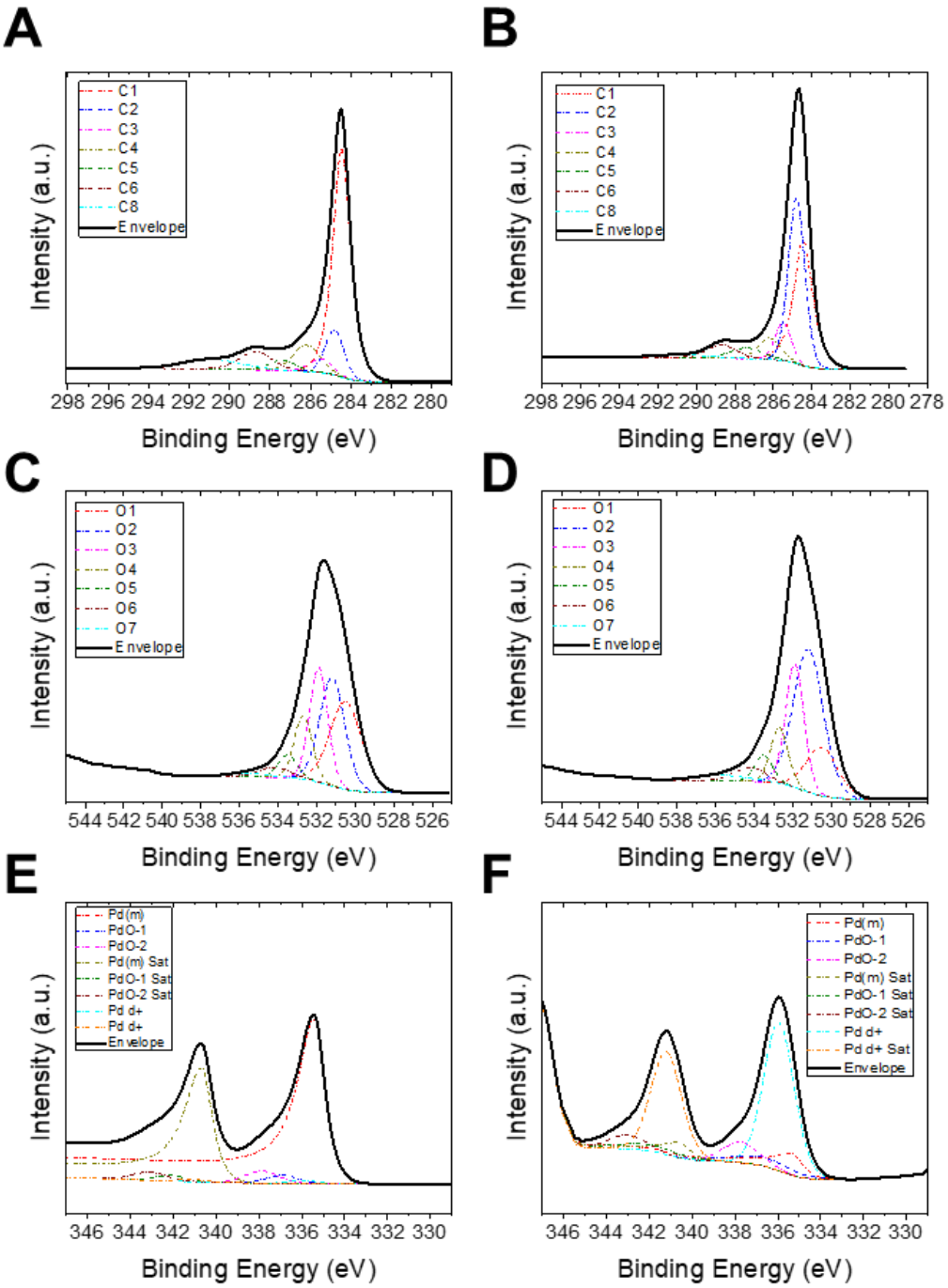

Fig. S18 XPS Spectra of Fresh and Spent Pd/C catalyst. (A) Fresh C1s region (B) Spent C1s region (C) Fresh O1s region (D) Spent O1s region (E) Fresh Pd region (F) Spent Pd region.

Fig. S19 displays the GC trace obtained from 6PPD hydroconversion. The products ID'ed (numbers labeled above peaks) were made with corresponding GCMS measurements and standards. Due to the lower temperature (150 °C vs 185 °C), the smaller end products, such as cyclohexylamine, do not form.

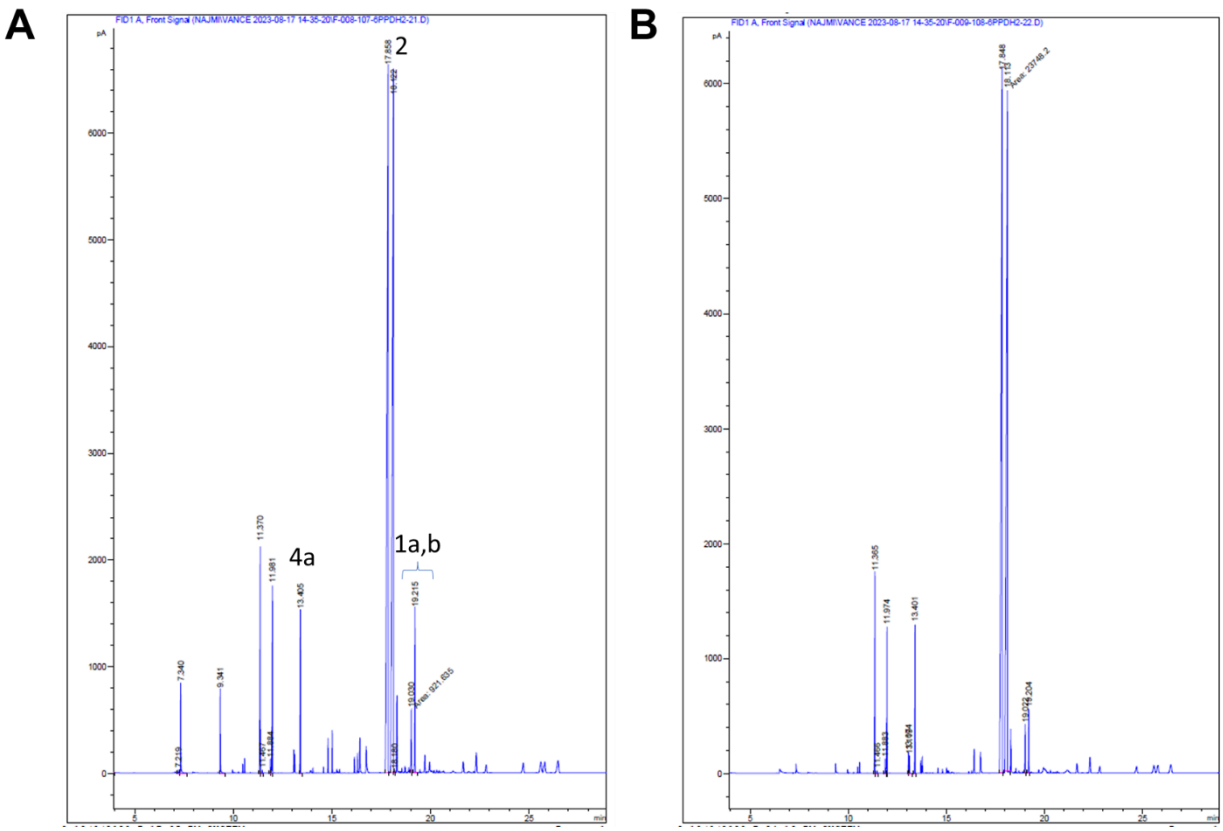

Fig. S19 GCFID results from 6PPD hydroconversion after (A) 1.5 h and (B) 3 h. Conditions: 1 g 6PPD, 20 mg Pd/C, 150 °C, P = 50 bar H_2.

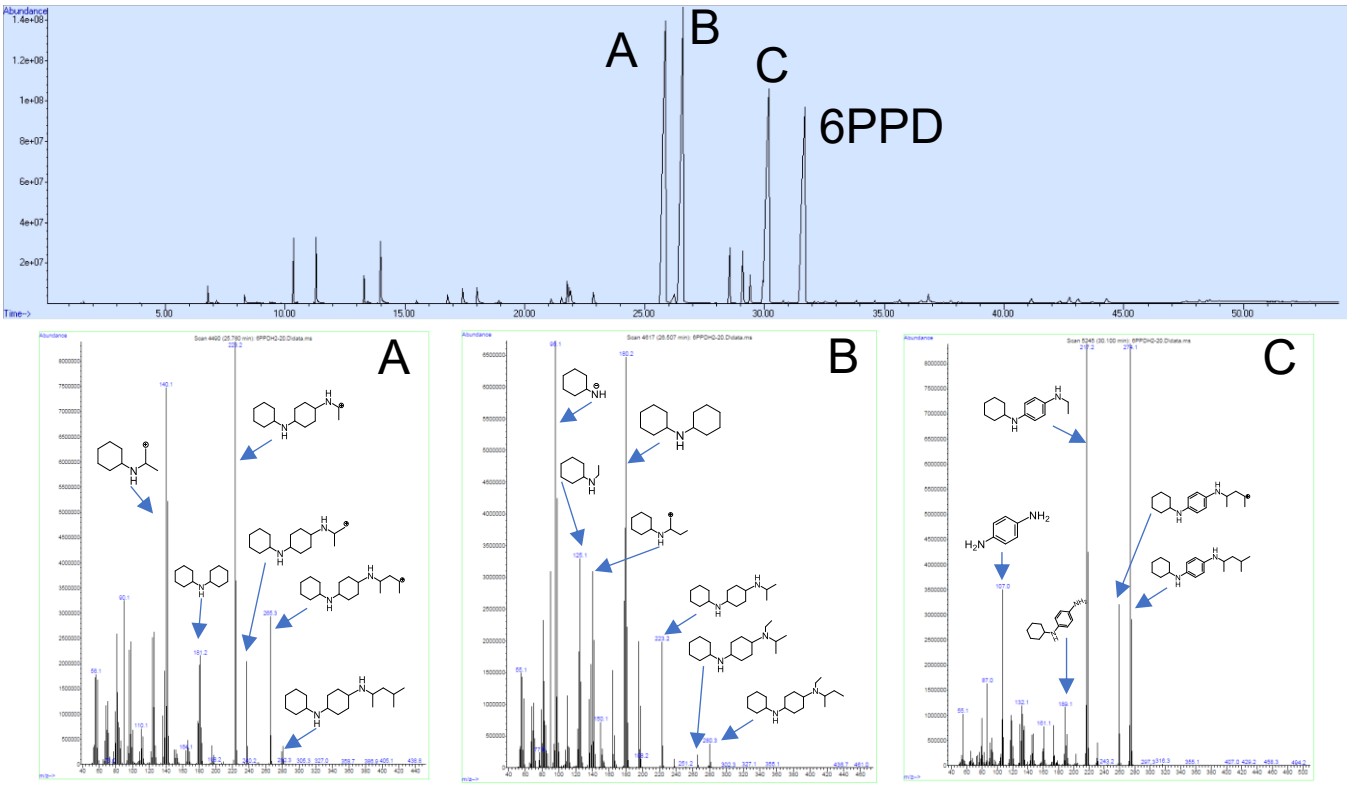

Fig. S20 GCMS Chromatogram and tandem mass spectra of products. Conditions: 150 °C, 45 min, 50 bar H2 (cold pressure), 20 mg Pd/C, 1 g 6PPD.

The hydroconversion of the extracted oil was tested to measure the efficacy of this catalyst on the real starting material. Full conversion of 6PPD was achieved after 30 min at 220 °C and 50 bar H_2 (cold pressure). GCMS was run on the product, and the resulting chromatogram with the mass spectrum is shown in Fig. S21. Dodecane (internal standard) and 2,2,4-trimethyl-1,2,3,4-tetrahydroquinoline were the only detectable products. The large fraction of remaining solid products (40%) suggests side reactions, where fatty acids and other compounds may form larger molecular weight products.

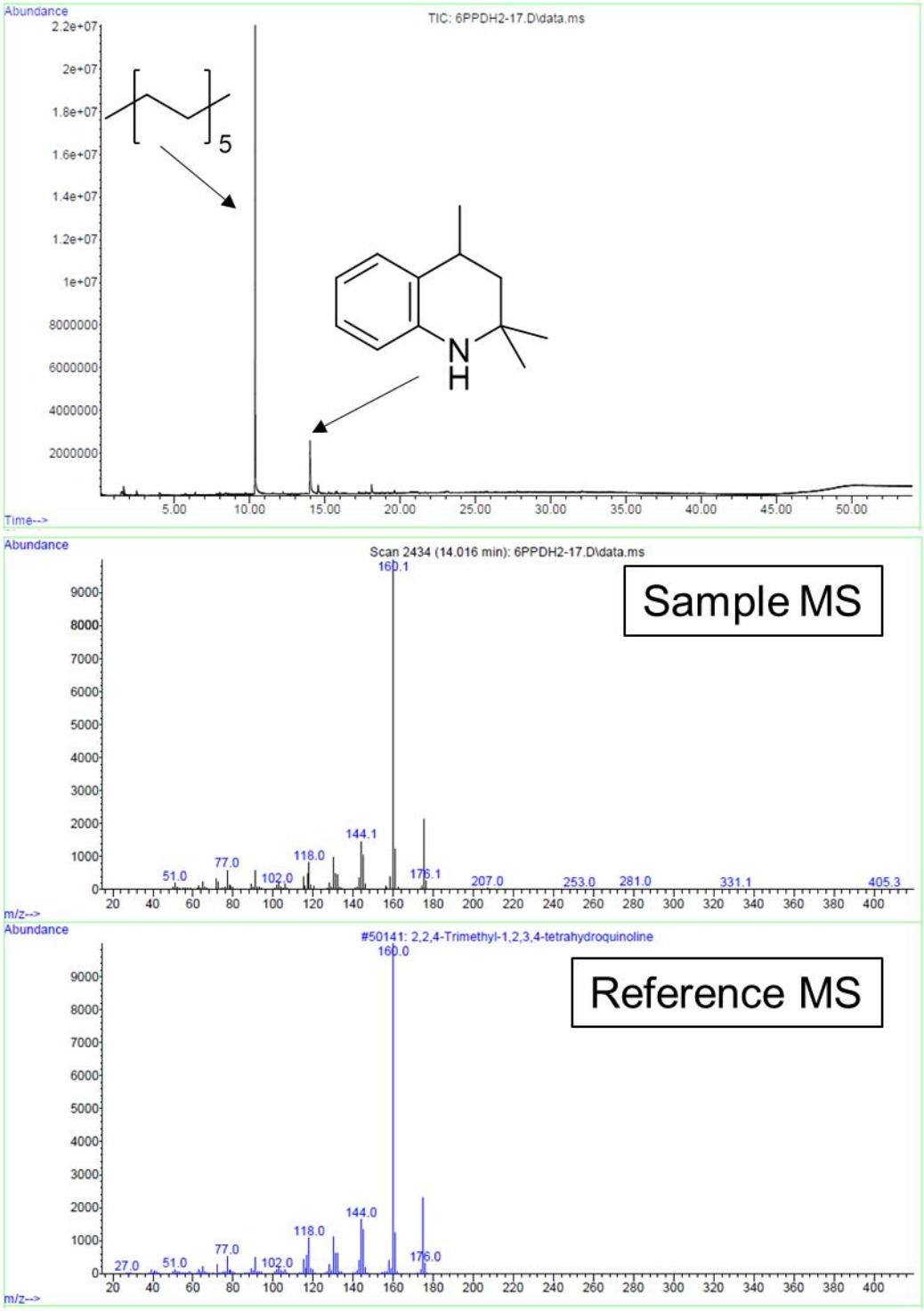

Fig. S21 GCMS from Hydroconversion of tire extract. The chromatogram from the product solution with the peaks indicating elution of dodecane and the product. The MS pattern from the sample's retention time and the reference from the NIST library are shown to confirm product identification.

A process simulation was developed to calculate costs. Flowrates for all streams are shown in Table S5. The corresponding process flowsheet with labeled streams is provided in Fig. S22.

Table S5 Mass flow rates for labeled streams corresponding to XX

Compounds	STREAMS (kg/hr)																			
	CBLACK	CRPYRO	CRSALE	FRESHSOL	HSOL	HSOLTIRE	HTIRE	PPD	PPDAD	PYROOIL	PYROPROD	S1	S2	S3	SBR	SOLREC	SOLTIRE	SOLUSED	SOLVENT	TIRE	WASTE
TOTAL FLOW	242.83	2535.48	2535.48	3.38	33.76	137.25	5174.4	103.49	103.49	2292.66	2535.48	113.49	10	103.49	5070.96	33.76	137.25	30.39	33.76	5174.45	3.38
Acetone	0	0	0	3.38	33.76	33.76	0	0	0	0	0	0	0	0	0	33.76	33.76	30.39	33.76	0	3.38
SBR	0	950.81	950.81	0	0	0	1901.61	0	0	0	0	0	0	0	1901.61	0	0	0	0	1901.61	0
6PPD	0	0	0	0	0	103.49	103.49	103.49	103.49	0	0	19.29	0	103.49	0	0	103.49	0	0	103.49	0
cyclohexane	0	0	0	0	0	0	0	0	0	0	0	7.94	0	0	0	0	0	0	0	0	0
cyclohexylamine	0	0	0	0	0	0	0	0	0	0	0	79.44	0	0	0	0	0	0	0	0	0
Dimethyl lbutylamine	0	0	0	0	0	0	0	0	0	0	0	2.27	0	0	0	0	0	0	0	0	0
Dicyclo hexylamine	0	0	0	0	0	0	0	0	0	0	0	4.54	0	0	0	0	0	0	0	0	0
hydrogen	0	0	0	0	0	0	0	0	0	0	0	0	10	0	0	0	0	0	0	0	0
benzene	0	0	0	0	0	0	0	0	0	96.69	96.69	0	0	0	0	0	0	0	0	0	0
toluene	0	0	0	0	0	0	0	0	0	372.56	372.56	0	0	0	0	0	0	0	0	0	0
m-xylene	0	0	0	0	0	0	0	0	0	232.16	232.16	0	0	0	0	0	0	0	0	0	0
o-xylene	0	0	0	0	0	0	0	0	0	96.37	96.37	0	0	0	0	0	0	0	0	0	0
p-xylene	0	0	0	0	0	0	0	0	0	232.16	232.16	0	0	0	0	0	0	0	0	0	0
ethylbenzene	0	0	0	0	0	0	0	0	0	52.56	52.56	0	0	0	0	0	0	0	0	0	0
styrene	0	0	0	0	0	0	0	0	0	322.29	322.29	0	0	0	0	0	0	0	0	0	0
limonene	0	0	0	0	0	0	0	0	0	854.39	854.39	0	0	0	0	0	0	0	0	0	0
carbon black	242.83	1267.74	1267.74	0	0	0	2535.48	0	0	0.00	242.83	0	0	0	2535.48	0	0	0	0	2535.48	0
butadiene	0	316.94	316.94	0	0	0	633.87	0	0	33.48	33.48	0	0	0	633.87	0	0	0	0	633.87	0

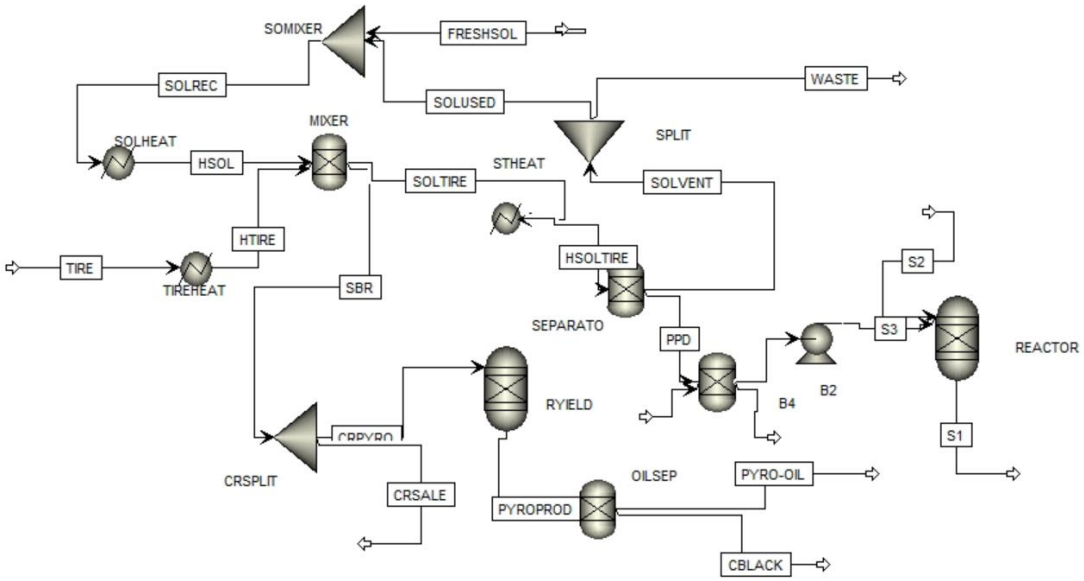

Fig. S22 Process flowsheet developed in ASPEN Plus modeling suite (V12).

The mass fraction of 6PPD and 6PPD-Q in relevant solvents is shown in Table S6. All values were calculated using COSMO-RS. Interestingly, across all solvents, the mass fraction for the quinone structure is several orders of magnitude lower than the parent structure. As expected, the mass fraction in water is meager but corroborates the concentrations observed by Tian et al.[20]. The significant drop in mass fraction from 6PPD to 6PPD-Q in hexane suggests the loss in aromaticity greatly reduces the dissolution of this compound.

Table S6 Mass fractions of 6PPD and 6PPD-Q in various solvents calculated by COSMO-RS.

Solvent	6PPD	6PPD-Q
1-Butanol	0.608856	0.003559
Ethyl Acetate	0.684849	0.00178
Acetone	0.790181	0.017888
Methanol	0.64937	0.005366
Isopropyl Alcohol	0.674684	0.00619
Ethanol	0.673157	0.006068
Water	1.48E-07	6.18E-08
2-hexanone	0.69988	0.00575
Hexane	0.30831	6.98E-08
1-propanol	0.663955	0.005335
MiBK	0.673543	0.001798
butanone	0.754338	0.010117
GVL	0.646043	0.001721
2-Butanol	0.612486	0.003297
Acetonitrile	0.267594	0.000281

The crumb rubber's particle size affects the bed's height when used in the tubular, continuous flow setup (Fig. S23). The bed was packed by filling the tube and gently tapping the tube bottom several times. As

expected, packing the bed results in a higher overall bed density. The larger particles are denser, resulting in a denser bed, although the changes in packing are not as significant as with the smaller particles. Based on these measurements, the calculated void fractions (Ɛ) in the packed beds are 0.17 for the larger particles and 0.06 for the smaller particles. These are rather low values.

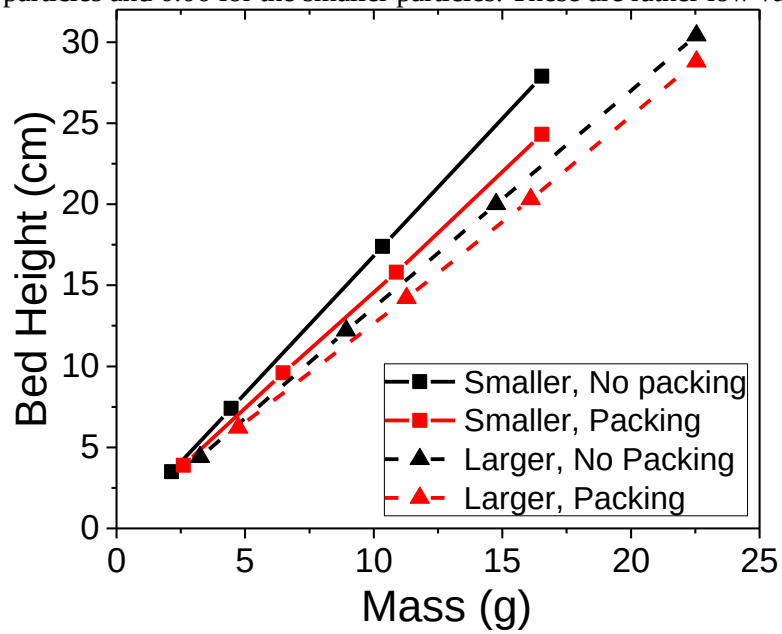

Fig. S23 Bed height of crumb for the smaller (0.6 mm) and larger (1.3 mm) particle sizes with and without bed packing.

The H_2 TPR of the 5 wt% Pd/C catalyst shown in Fig. S24 shows two different peaks at 68 and 80 °C. These two peaks are attributed to Pd clusters of different sizes[21].

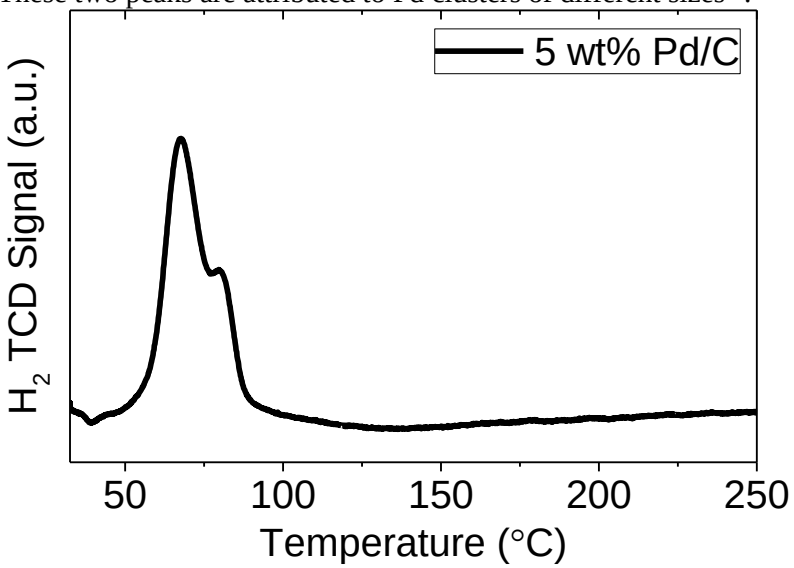

Fig. S24 Hydrogen Temperature programmed reduction of 5 wt% Pd/C catalyst.

The N_2 isotherm is shown in Fig. S25 and displays a type II adsorption shape. The high surface area measured is typically of other carbon-based catalysts[22].

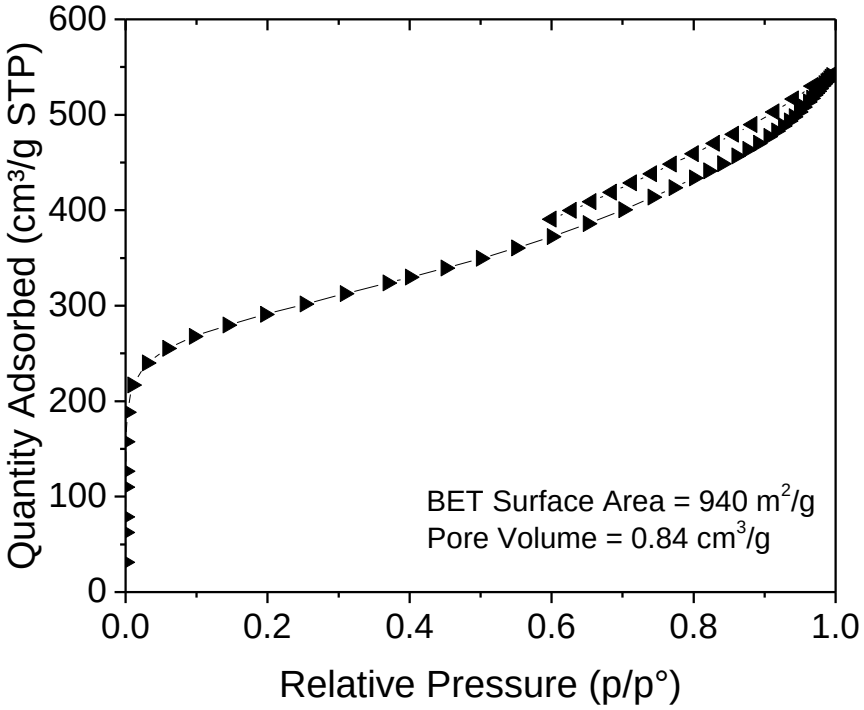

Fig. S25 N_2 Physisorption isotherm of the 5 wt % Pd/C catalyst.

Hydrogen partial pressure significantly affects the conversion of 6PPD (Fig. S26). This is due to the two aromatic rings present in the 6PPD structure, which require large amounts of hydrogen to be fully transformed into another product. The conversion and amount of hydrogen consumed are roughly the same between the 40:10 H_2: He and 50:0 H_2: He experiments. This suggests 40 bar H_2 may be sufficient to convert 6PPD at the given conditions.

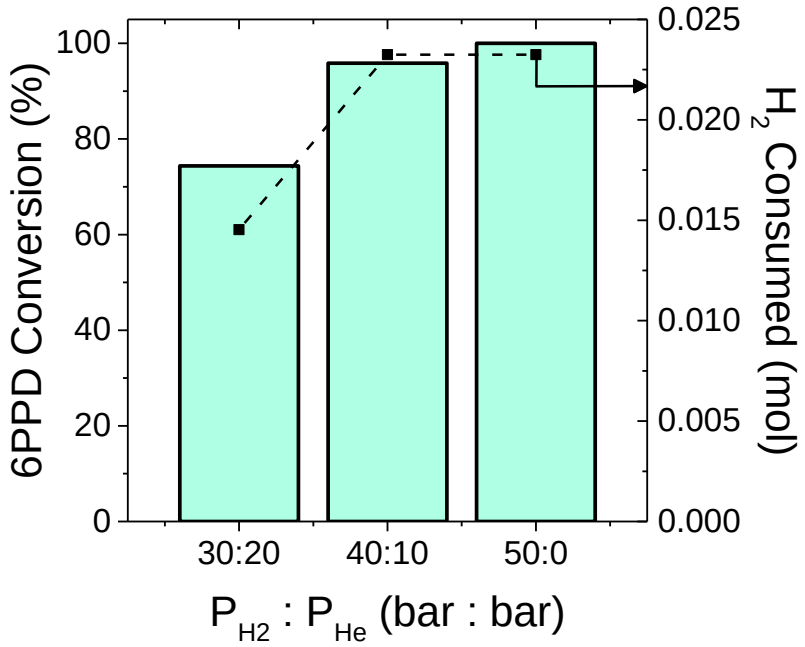

Fig. S26 Conversion of 6PPD as a function of hydrogen partial pressure. Conditions 150 °C, 1.5 h, 1 g 6PPD and 20 mg Pd/C.

References

1. Gutierrez-Cano, J. D. *et al.* A New Stand-Alone Microwave Instrument for Measuring the Complex Permittivity of Materials at Microwave Frequencies. *IEEE Trans Instrum Meas* **69**, 3595–3605 (2020).
2. Baker-Fales, M., Chen, T.-Y. & Vlachos, D. G. Scale-up of microwave-assisted, continuous flow, liquid phase reactors: Application to 5-Hydroxymethylfurfural production. *Chemical Engineering Journal* **454**, 139985 (2023).
3. Martin, T. M., Harten, P., Venkatapathy, R., Das, S. & Young, D. M. A hierarchical clustering methodology for the estimation of toxicity. *Toxicol Mech Methods* **18**, 251–266 (2008).
4. Young, D., Martin, T., Venkatapathy, R. & Harten, P. Are the chemical structures in your QSAR correct? *QSAR Comb Sci* **27**, 1337–1345 (2008).
5. Pye, C. C., Ziegler, T., Lenthe, E. Van & Louwen, J. N. An implementation of the conductor-like screening model of solvation within the amsterdam density functional package - Part II. COSMO for real solvents. *Can J Chem* **87**, 790–797 (2009).
6. Selvam, E. *et al.* Plastic waste upgrade to olefins via mild slurry microwave pyrolysis over solid acids. *Chemical Engineering Journal* **454**, 140332 (2023).
7. Jansen, R. J. J. & Van Bekkum, H. XPS OF NITROGEN-CONTAINING FUNCTIONAL GROUPS ON ACTIVATED CARBON. *Carbon N Y* **33**, 1021–1027 (1995).
8. Wang, J. *et al.* Breaking the lattice match of Pd on Au(111) nanowires: Manipulating the island and epitaxial growth pathways to boost the oxygen reduction reactivity. *J Mater Chem A Mater* **8**, 19300–19308 (2020).
9. Dutta, S. *et al.* Solventless C-C Coupling of Low Carbon Furanics to High Carbon Fuel Precursors Using an Improved Graphene Oxide Carbocatalyst. *ACS Catal* **7**, 3905–3915 (2017).
10. Blume, R. *et al.* Characterizing Graphitic Carbon with X-ray Photoelectron Spectroscopy: A Step-by-Step Approach. *ChemCatChem* **7**, 2871–2881 (2015).
11. Reiche, S. *et al.* Reactivity of mesoporous carbon against water - An in-situ XPS study. *Carbon N Y* **77**, 175–183 (2014).
12. Friedel Ortega, K., Arrigo, R., Frank, B., Schlögl, R. & Trunschke, A. Acid-Base Properties of N-Doped Carbon Nanotubes: A Combined Temperature-Programmed Desorption, X-ray Photoelectron Spectroscopy, and 2-Propanol Reaction Investigation. *Chemistry of Materials* **28**, 6826–6839 (2016).
13. Rao, R. G. *et al.* Interfacial charge distributions in carbon-supported palladium catalysts. *Nat Commun* **8**, (2017).
14. Arrigo, R. *et al.* Pd Supported on Carbon Nitride Boosts the Direct Hydrogen Peroxide Synthesis. *ACS Catal* **6**, 6959–6966 (2016).
15. Cárdenas-Lizana, F. *et al.* Selective gas phase hydrogenation of p-chloronitrobenzene over Pd catalysts: Role of the support. *ACS Catal* **3**, 1386–1396 (2013).
16. Xie, S., Ji, Z., Yang, Y., Hou, G. & Wang, J. Electromagnetic wave absorption enhancement of carbon black/gypsum based composites filled with expanded perlite. *Compos B Eng* **106**, 10–19 (2016).
17. Simon, D. Á. & Bárány, T. Microwave Devulcanization of Ground Tire Rubber and Its Improved Utilization in Natural Rubber Compounds. *ACS Sustain Chem Eng* (2023) doi:10.1021/acssuschemeng.2c05984.

18. Song, Z. *et al.* Microwave pyrolysis of tire powders: Evolution of yields and composition of products. *J Anal Appl Pyrolysis* **123**, 152–159 (2017).
19. Bing, W. *et al.* Microwave fast pyrolysis of waste tires: Effect of microwave power on product composition and quality. *J Anal Appl Pyrolysis* **155**, 104979 (2021).
20. Tian, Z. *et al.* A ubiquitous tire rubber-derived chemical induces acute mortality in coho salmon. *Science (1979)* **371**, 185–189 (2021).
21. Zheng, X. *et al.* Deactivation of Pd/C catalysts in the hydrodechlorination of the chlorofluorocarbons CFC-115 and CFC-12. in *Catalysis Today* vol. 175 615–618 (Elsevier B.V., 2011).
22. Zhou, J. *et al.* Tuning the reactivity of carbon surfaces with oxygen-containing functional groups. *Nat Commun* **14**, (2023).